

Chapter 3

Shot-profile migration in elliptic coordinates

This chapter extends the Riemannian wavefield extrapolation (RWE) approach developed in Chapter 2 to 2D prestack migration using elliptical coordinate systems. I show that the corresponding 2D elliptical extrapolation wavenumber introduces only an isotropic slowness model stretch to the single-square-root operator. This enables the use of existing Cartesian finite-difference extrapolators for propagating wavefields on elliptical meshes. A post-stack migration example illustrates the advantages of elliptical coordinates for imaging with turning waves. A 2D imaging test using a velocity benchmark data set demonstrates that the RWE prestack migration algorithm generates high-quality migration images that are more accurate than those generated by Cartesian operators of the equivalent accuracy. I note that even in situations where RWE geometries are employed, a high-order implementation of the one-way extrapolator operator is required for accurate propagation and imaging. The results of this chapter are published as Shragge and Shan (2008).

INTRODUCTION

Wave-equation migration techniques based on one-way extrapolators are often used for accurate imaging of complex geologic structures. Most conventional downward continuation approaches, though, are unable to handle the steeply propagating or turning-wave components often important for imaging areas of interest. A number of novel imaging approaches address these issues through a judicious decomposition of recorded wavefields [e.g. plane-wave migration (Whitmore, 1995)], partial and complete propagation-domain decomposition [e.g. Gaussian beam migration (Hill, 2001) and Riemannian wavefield extrapolation (Sava and Fomel, 2005; Shragge, 2008), respectively], or a combination thereof [e.g. plane-wave migration in tilted coordinates (Shan and Biondi, 2004)]. These techniques have overcome many, though not all, issues in the practical application of one-way extrapolation operators.

Riemannian wavefield extrapolation (RWE) is a method for propagating wavefields on generalized coordinate meshes. The central idea of RWE is to transform the computational domain from Cartesian to a geometry where the extrapolation axis is oriented along the general wavefield propagation direction. Ideally, solving the corresponding one-way extrapolation equations in the transform domain leads to the bulk of wavefield energy being propagated at angles relatively near to the extrapolation axis, thus improving the global extrapolation accuracy. One obvious application is generating high-quality Green's functions for point-sources in a dynamic coordinate system, where a suite of rays is first traced through a velocity model and then used as the skeleton on which to propagate wavefields (see Chapter 1).

Although the full-domain decomposition approach naturally adapts to propagation in a point-source ray-coordinate system, two unresolved issues make it difficult to apply RWE efficiently in prestack shot-profile migration algorithms. First, receiver wavefields in shot-profile migration are usually broadband in plane-wave dip spectrum and cannot be easily represented by a single coordinate system (i.e. reflections from opposing dips propagate in opposing directions). Second, the optimal meshes for the

source and receiver wavefields usually do not share a common geometry. For example, a polar coordinate system is well-suited for propagating source wavefields, while elliptical meshes are more appropriate for receiver wavefields. This factor is detrimental to algorithmic efficiency where images are generated by correlating source and receiver wavefields: by existing on different grids they must both be interpolated to a common Cartesian reference frame prior to imaging. This leads to a significant number of interpolations, which leaves the algorithm computationally unattractive, except in target-oriented imaging situations.

The main goal of this chapter is to specify a single coordinate system that enables the accurate propagation of large-angle and turning-wave components of both the source and receiver wavefields. I demonstrate that an elliptical coordinate system forms a natural computational grid for prestack shot-profile migration and has useful geometric properties that facilitate numerical implementation. An elliptical coordinate system originates on the horizontal acquisition surface and steps outward as a series of ellipses. Thus, the coordinate system expands in a radial-like manner appropriate for computing accurate point-source Green's functions while allowing the dipping plane-wave components in the receiver wavefield to propagate at large angles to either side of the acquisition surface. One consequence of using a 2D elliptical coordinate system is that the corresponding extrapolation operator must be modified; however, I show that elliptical geometry introduces only an isotropic velocity model stretch. Existing high-order implicit Cartesian finite-difference extrapolation operators with accuracy up to 80° from the extrapolation axis (Lee and Suh, 1985) can be used to propagate wavefields, readily enabling accurate imaging of large-angle and turning waves at a cost competitive with that of Cartesian downward continuation.

This chapter begins with a discussion of why elliptical meshes are a natural coordinate system choice for shot-profile prestack depth migration (PSDM). I develop an extrapolation wavenumber appropriate for wavefield propagation on 2D elliptical coordinate systems. I then present post-stack and prestack migration examples that illustrate the scheme's ability to image steep structure using turning waves. The chapter concludes with a discussion on the advantages of analytic coordinate systems

relative to more dynamically generated meshes.

ELLIPTIC COORDINATE EXTRAPOLATION

Generating an effective RWE coordinate system for prestack migration requires appropriately linking mesh geometry with wavefield propagation kinematics. Figure 4.1 illustrates this concept for an idealized shot-profile imaging experiment through a medium of constant slowness s . Here, I specify source and receiver wavefields (S and R) as impulses at source position and time $[\mathbf{x}_s, \tau_s = 0]$ and at receiver position and time $[\mathbf{x}_r, \tau_r = \tau]$, where τ is an arbitrary time lag. The wavefields expand outward as spherical wavefronts (dashed lines) according to

$$S(\mathbf{x}_s, \mathbf{x}|t) = \delta(t - s\|\mathbf{x} - \mathbf{x}_s\|) \quad \text{and} \quad R(\mathbf{x}_r, \mathbf{x}|t) = \delta(t - \tau + s\|\mathbf{x} - \mathbf{x}_r\|), \quad (3.1)$$

where $\|\mathbf{x}\|$ is the Euclidean norm of the vector \mathbf{x} and s is slowness. An image $I(\mathbf{x})$ can be generated by applying a correlation imaging condition at $t = 0$ (Claerbout, 1985),

$$I(\mathbf{x}) = \delta(\tau - s(\|\mathbf{x} - \mathbf{x}_r\| + \|\mathbf{x} - \mathbf{x}_s\|)), \quad (3.2)$$

which is the equation of an ellipse (solid line).

This suggests a natural correspondence between an elliptical coordinate system and the prestack migration isochrons for a constant velocity model. One can observe this in Figure 4.1a by how well the isochron image conforms to the underlying coordinate mesh. In this example, I intentionally did not fix the locations of the elliptical mesh foci relative to \mathbf{x}_s and \mathbf{x}_r . Adjusting these points will alter both the elliptical mesh and how well it conforms to the isochrons. These parameters represent two degrees of freedom that allow better tuning of mesh geometry to the bulk propagation direction.

The Helmholtz equation in elliptical coordinates

As demonstrated in Chapter 2, propagating a wavefield U in generalized coordinates requires encoding the mesh geometry directly into the one-way extrapolation equations (Sava and Fomel, 2005; Shragge, 2008). Hence, deriving an elliptical-coordinate extrapolation operator requires introducing elliptical geometry into the Laplacian operator ∇^2 of the Helmholtz equation,

$$\nabla^2 U + \omega^2 s^2 U = 0. \quad (3.3)$$

where U is either a source or receiver wavefield. I begin with the definition of the analytic transformation between the elliptical and Cartesian coordinate systems (Morse and Feshbach, 1953),

$$\begin{bmatrix} x_1 \\ x_3 \end{bmatrix} = \begin{bmatrix} a \cosh \xi_3 \cos \xi_1 \\ a \sinh \xi_3 \sin \xi_1 \end{bmatrix}, \quad (3.4)$$

where $\mathbf{x} = [x_1, x_3]$ are the underlying Cartesian coordinate variables, $\boldsymbol{\xi} = [\xi_1, \xi_3]$ are the RWE elliptical coordinates defined on the intervals $\xi_1 \in [0, \pi)$, and $\xi_3 \in [0, \infty]$, and a is a stretch parameter controlling coordinate system breadth. Herein, $x_2 = \xi_2 = 0$ are assumed. As illustrated in Figure 4.1, lines of constant ξ_3 represent ellipses, while those of constant ξ_1 form hyperbolas. Figure 4.1 illustrates the angle convention used herein, where $\theta(\boldsymbol{\xi})$ represents the angle between the elliptical extrapolation direction and the vertical axis of the Cartesian coordinate system. Additional information on the physical interpretation of elliptical coordinates is presented in Appendix D.

The metric tensor ($g_{jk} = \frac{\partial x_l}{\partial \xi_j} \frac{\partial x_l}{\partial \xi_k}$ with an implicit sum over index l) describing elliptical coordinates is

$$[g_{jk}] = \begin{bmatrix} A^2 & 0 \\ 0 & A^2 \end{bmatrix}, \quad (3.5)$$

where $A = a\sqrt{\sinh^2 \xi_3 + \sin^2 \xi_1}$. The metric tensor determinant, $|\mathbf{g}| = A^4$, is required

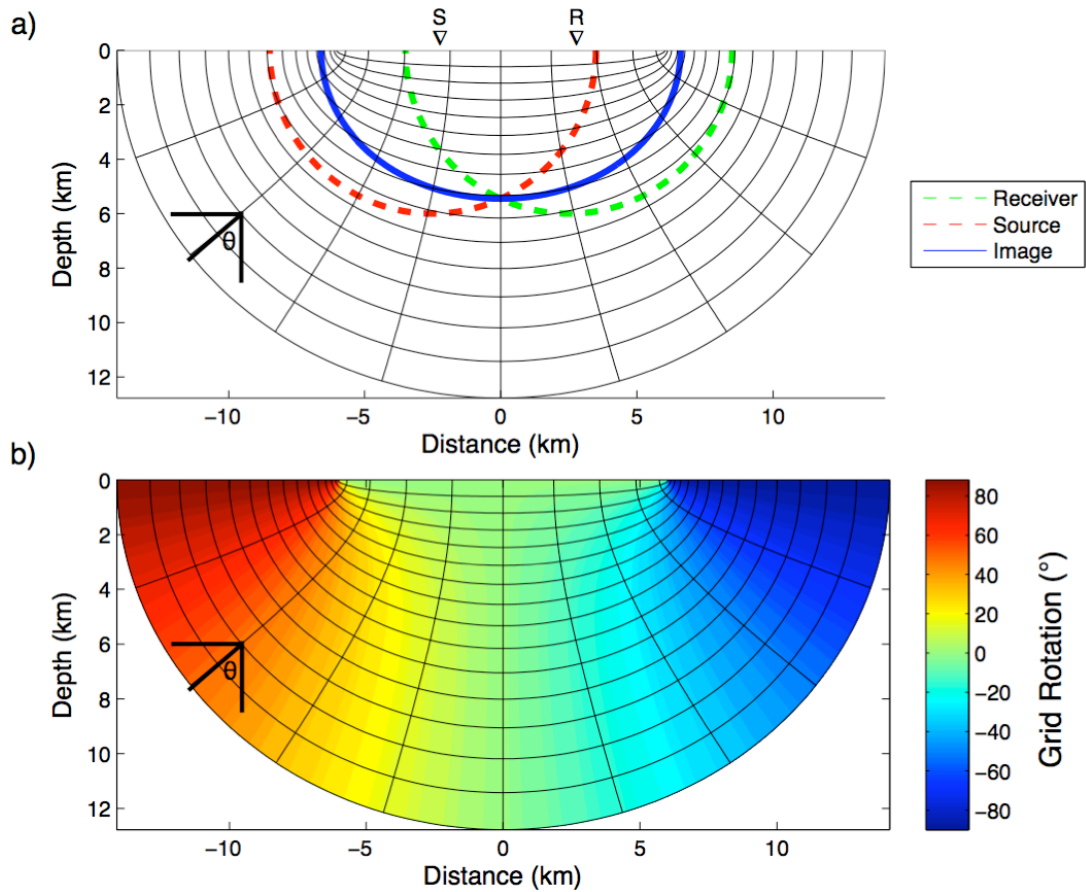


Figure 3.1: Illustrating the elliptical coordinate system. a) Constant-velocity imaging experiment with point source and receiver wavefields (dashed lines) from locations marked S and R , respectively. The corresponding image is an elliptical isochron surface derived by cross-correlating the source and receiver wavefields (solid line). b) Grid rotation angles for the elliptical coordinate system with respect to the vertical Cartesian depth axis. **NR** `georwe/. Figure1`

to specify the weighted metric tensor, m^{jk} ,

$$[m^{jk}] = \begin{bmatrix} 1 & 0 \\ 0 & 1 \end{bmatrix}. \quad (3.6)$$

Importantly, the weighted metric tensor m^{jk} in equation 3.6 is an identity matrix, indicating that the transformation in equation 3.4 causes space to contract or dilate isotropically.

Following the development in Chapter 2, I insert the tensor components in equations 3.6 into the standard expression for the Laplacian operator (Morse and Feshbach, 1953),

$$\nabla^2 = \frac{1}{\sqrt{|\mathbf{g}|}} \frac{\partial}{\partial \xi_j} \left(m^{jk} \frac{\partial}{\partial \xi_k} \right), \quad (3.7)$$

which leads to the elliptical coordinate Laplacian operator,

$$\nabla^2 = \frac{1}{A^2} \left(\frac{\partial^2}{\partial \xi_1^2} + \frac{\partial^2}{\partial \xi_3^2} \right). \quad (3.8)$$

The elliptical coordinate Helmholtz equation is derived by introducing equation 3.8 into equation 3.3 and rearranging terms to yield

$$\left[\frac{\partial^2}{\partial \xi_1^2} + \frac{\partial^2}{\partial \xi_3^2} \right] U + A^2 \omega^2 s^2 U = 0. \quad (3.9)$$

Defining an effective slowness field $s_{eff} = As$ changes the above to

$$\left[\frac{\partial^2}{\partial \xi_1^2} + \frac{\partial^2}{\partial \xi_3^2} \right] U + \omega^2 s_{eff}^2 U = 0. \quad (3.10)$$

Equation 3.10 is the most important result in Chapter 2: elliptical coordinates introduce only an isotropic slowness model stretch in the Helmholtz equation.

Dispersion relation in elliptical coordinates

Deriving an elliptical-coordinate dispersion relation from equation 3.10 proceeds in the usual manner (Claerbout, 1985). The following 2D development uses a convention where ξ_3 and ξ_1 are the extrapolation direction and orthogonal coordinate, respectively. Replacing the partial differential operators with their Fourier domain duals, gives

$$k_{\xi_1}^2 + k_{\xi_3}^2 = \omega^2 s_{eff}^2, \quad (3.11)$$

and isolating the k_{ξ_3} wavenumber contributions leads to a wavefield extrapolation operator for recursive outward stepping in concentric ellipses in the ξ_3 direction,

$$U(\xi_3 + \Delta\xi_3, k_{\xi_1}|\omega) = U(\xi_3, k_{\xi_1}|\omega)e^{\pm i\Delta\xi_3 k_{\xi_3}} = U(\xi_3, k_{\xi_1}|\omega)e^{\pm i\Delta\xi_3 \sqrt{\omega^2 s_{eff}^2 - k_{\xi_1}^2}}, \quad (3.12)$$

where $\Delta\xi_3$ is the extrapolation step size, and \pm determines whether a wavefield is propagating causally or acausally (i.e. source and receiver wavefields, respectively).

The dispersion relation in equation 3.12 will not be an exact expression in general because s_{eff} varies spatially. This situation is similar to that in Cartesian wavefield extrapolation in laterally varying media, and equation 3.12 can be easily implemented with existing Cartesian extrapolation schemes (e.g. finite differences, PSPI) using an effective slowness model $s_{eff} = As$.

An additional question worth addressing is to which angle is propagation in elliptical coordinates accurate? Because the geometric effects of elliptical coordinates can be incorporated into an effective slowness model, s_{eff} , the local angular accuracy for finite-difference propagation is equivalent to that of the Cartesian-domain implementation. Globally, though, the maximum propagation angle for a given extrapolation accuracy depends on the orientation of the local extrapolation axis. Figure 4.1b illustrates how the angle of the extrapolation axis, $\theta = \theta(\boldsymbol{\xi})$, locally changes in elliptical coordinates with respect to the Cartesian depth axis. The following examples were generated with $\pm 80^\circ$ finite-difference propagators (Lee and Suh, 1985), and will have a maximum extrapolation angle equal to $\theta(\boldsymbol{\xi}) \pm 80^\circ$.

Prestack migration algorithm

The expression in equation 3.12 can be extended to prestack migration. An initial step is defining the foci locations of the elliptical coordinate system. Unfortunately, choosing the optimal location, relative to the acquisition geometry (i.e. the source and farthest-offset receiver locations), is not straightforward. For example, situating foci too close together pulls the wavefields towards the focus because the local extrapolation axis angle rapidly becomes steep (c.f. Figure 4.1b). In contrast, placing foci too distant from each other leads to a near-rectilinear coordinate system that affords little improvement over Cartesian extrapolation. I determined heuristically that optimal foci locations are an additional 10–20% (of the aperture length) beyond the source point and farthest receiver offset.

The remaining prestack migration algorithmic steps are:

1. Specify a shot-specific elliptical coordinate system for source location s_l , and interpolate the Cartesian velocity model to this mesh;
2. Generate the shot-specific image, $I(\boldsymbol{\xi}|s_l)$, in the elliptical coordinate system at step ξ_3 from the source, S , and receiver, R , wavefields

$$I(\boldsymbol{\xi}|s_l) = \sum_{\omega} \Re[S^*(\boldsymbol{\xi}|\omega, s_l)R(\boldsymbol{\xi}|\omega, s_l)]; \quad (3.13)$$

3. Propagate source and receiver wavefields (for all frequencies) by a step $\Delta\xi_3$

$$\begin{aligned} S(\xi_3 + \Delta\xi_3, k_{\xi_1}|\omega, s_l) &= S(\xi_3, k_{\xi_1}|\omega, s_l) e^{+i\Delta\xi_3 k_{\xi_3}}, \\ R(\xi_3 + \Delta\xi_3, k_{\xi_1}|\omega, s_l) &= R(\xi_3, k_{\xi_1}|\omega, s_l) e^{-i\Delta\xi_3 k_{\xi_3}}; \end{aligned} \quad (3.14)$$

4. Repeat steps 2-3 until reaching the end of the elliptical coordinate mesh;
5. Interpolate the single-shot, elliptical-coordinate image $I(\boldsymbol{\xi}|s_l)$ to Cartesian coordinates and update the global Cartesian image $I(\boldsymbol{x})$; and
6. Repeat steps 1-5 for all shot locations.

2D MIGRATION TESTS

This section presents 2D test results for a post-stack turning-wave and the prestack velocity benchmark (Billette and Brandsberg-Dahl, 2005) data sets. I propagate all wavefields with the one-way extrapolators described in Lee and Suh (1985) on an elliptical coordinate system defined by equation 3.4 assuming effective slowness fields $s_{eff} = As$. Imaging results are generated using post-stack and shot-profile migration algorithms employing the recursive extrapolation relations in equations 3.12 and 3.14, respectively. Image volumes in elliptical coordinates are transformed back to the Cartesian domain using sinc interpolation. The extra computational cost of generating the RWE migration results, relative to those in Cartesian imaging, is roughly two additional interpolations per shot: one for the Cartesian velocity model to the elliptical mesh, and another for the elliptical image to the Cartesian grid.

Post-stack migration example

The first elliptical coordinate migration example uses the post-stack data set shown in Figure 4.2. The data were generated from an adapted Sigsbee model, shown in

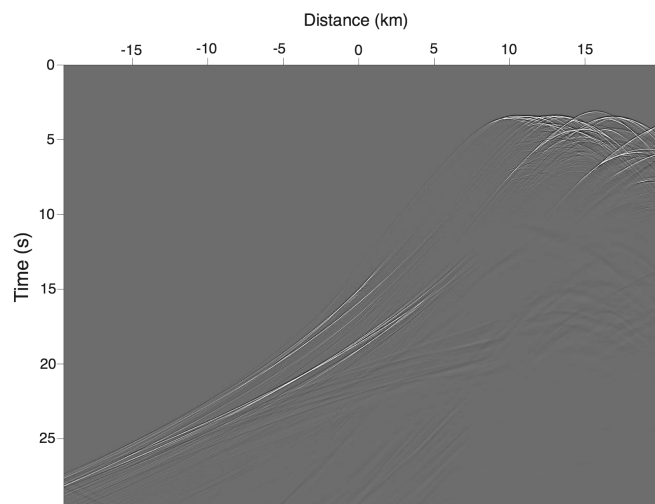


Figure 3.2: Post-stack turning-wave data generated by two-way time-domain finite-difference modeling from all salt body edges of the velocity model in Figure 4.3a. **ER** georwe/. Figure2

Figure 4.3a, using exploding reflector (two-way time-domain FD) modeling from all

salt body edges (Sava, 2006). The imaging test involved only the turning components of the wavefield shown in Figure 4.2. Figure 4.3a also presents the experimental

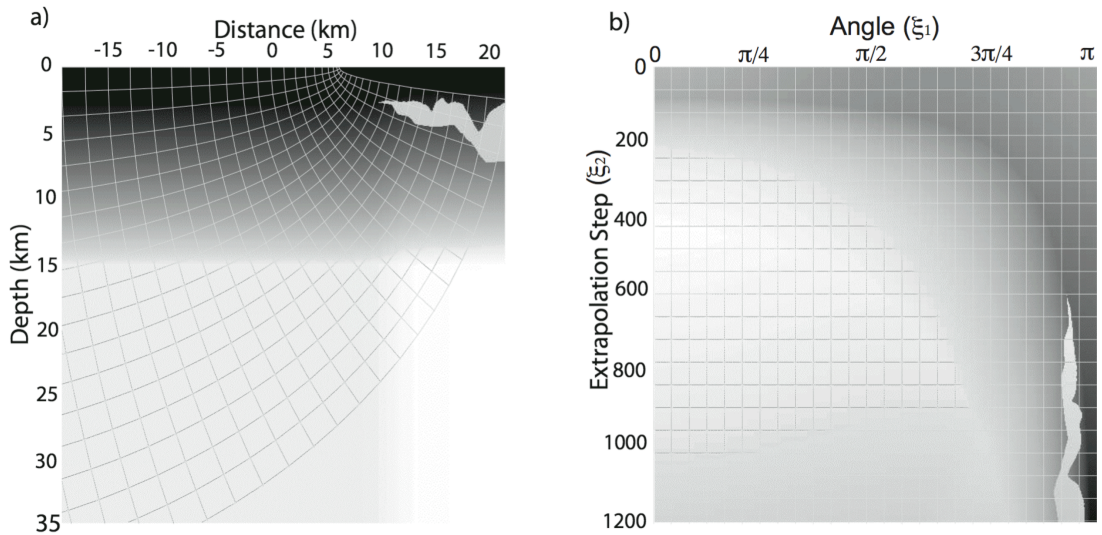


Figure 3.3: Post-stack turning-wave model. a) Velocity model used to generate turning wave data in Figure 4.2 with coordinate system overlain. b) Effective slowness model s_{eff} in elliptical coordinates. **ER** georwe/. Figure3

geometry for the coordinate system with foci situated at -90 km (not shown) and 5 km. Because the wavefield propagation directions are largely known, I chose foci locations that ensured a conformal grid. (I recognize that this example is a special case where the dip field is oriented largely in one direction.) Figure 4.3b shows the effective slowness model, s_{eff} , in the transformed coordinate system parameterized by extrapolation step and surface take-off position axes.

Figure 4.4 presents the results for migration in the chosen RWE elliptical coordinates. Panel 4.4a shows the monochromatic post-stack migration result with the elliptical coordinate system overlain. Note that the monochromatic wavefields illustrate that the propagation paths of wavefield energy are fairly conformal to the elliptical coordinate mesh. This demonstrates that post-stack migration in elliptical coordinates can successfully propagate turning waves, which, in this case, arrive at normal incidence to the salt flank as expected for exploding-reflector modeling. Panel 4.4b

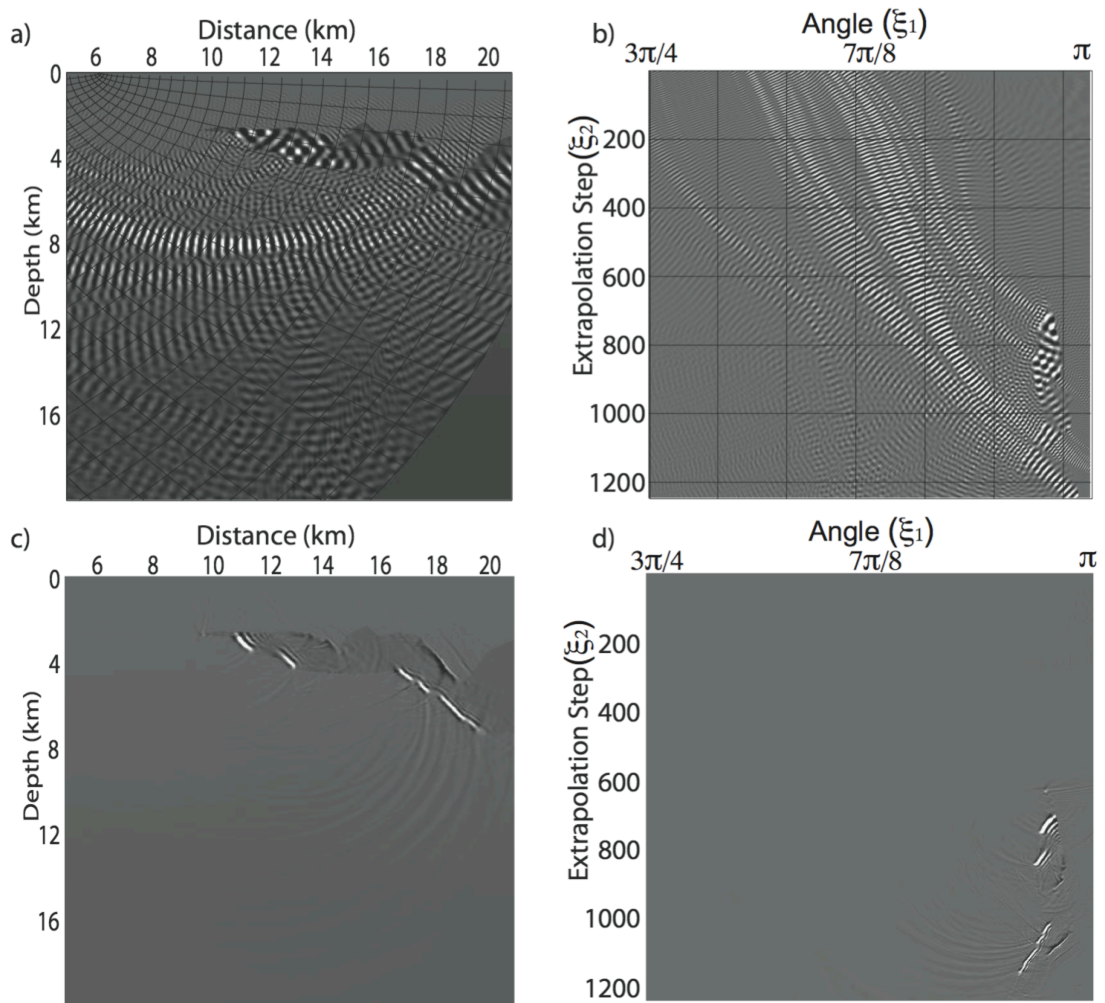


Figure 3.4: Post-stack turning-wave migration results. a) Monochromatic Cartesian image with overlain elliptical coordinates showing the wave-propagation paths. b) Monochromatic elliptical coordinate image. c) Broadband Cartesian image. d) Broadband elliptical coordinate image. **CR** georwe/. Figure4

shows the elliptical-coordinate version of the image in panel 4.4a at successive extrapolation steps, and illustrates that wavefield energy propagates at large angles relative to the extrapolation axis. Panels 4.4c and 4.4d show the broadband images for Cartesian and elliptical coordinate systems, respectively. The salt flanks beneath the salt nose are accurately positioned, demonstrating the potential for imaging with turning waves in elliptical coordinates using large-angle extrapolation operators.

Prestack migration example

I performed a prestack elliptical coordinate migration test using a velocity benchmark model (Figure 4.5a). Full data offsets were not used for each shot; rather, I used a 10 km initial migration aperture to enable more accurate propagation of turning waves within the propagation domain. I located the foci for each migrated shot an additional 15% (of the 10 km acquisition aperture) beyond the shot point and the farthest receiver offset. Panel 4.5b shows the effective slowness model, s_{eff} , in the elliptical coordinate system. The elliptical mesh is again parameterized by extrapolation step and surface take-off position axes. Importantly, the steep salt body structure to the right becomes relatively low angle under this coordinate transformation, and should be better imaged in elliptical coordinates.

Figure 4.6 presents the prestack migration results for the elliptical coordinate system. Panel 4.6a shows the RWE shot-profile migration result in elliptical coordinates, while panel 4.6b presents the corresponding Cartesian image generated by finite-difference operators of equivalent accuracy. (Note that slightly different source wavelets were used leading to a phase rotation between the two images.) The salt body to the left is well-imaged in most areas in both images, though is improved, for example, in the circled location in elliptical coordinates. The salt body flanks to the right (circled locations), illuminated largely by turning and prismatic waves, are better imaged in elliptical coordinates.

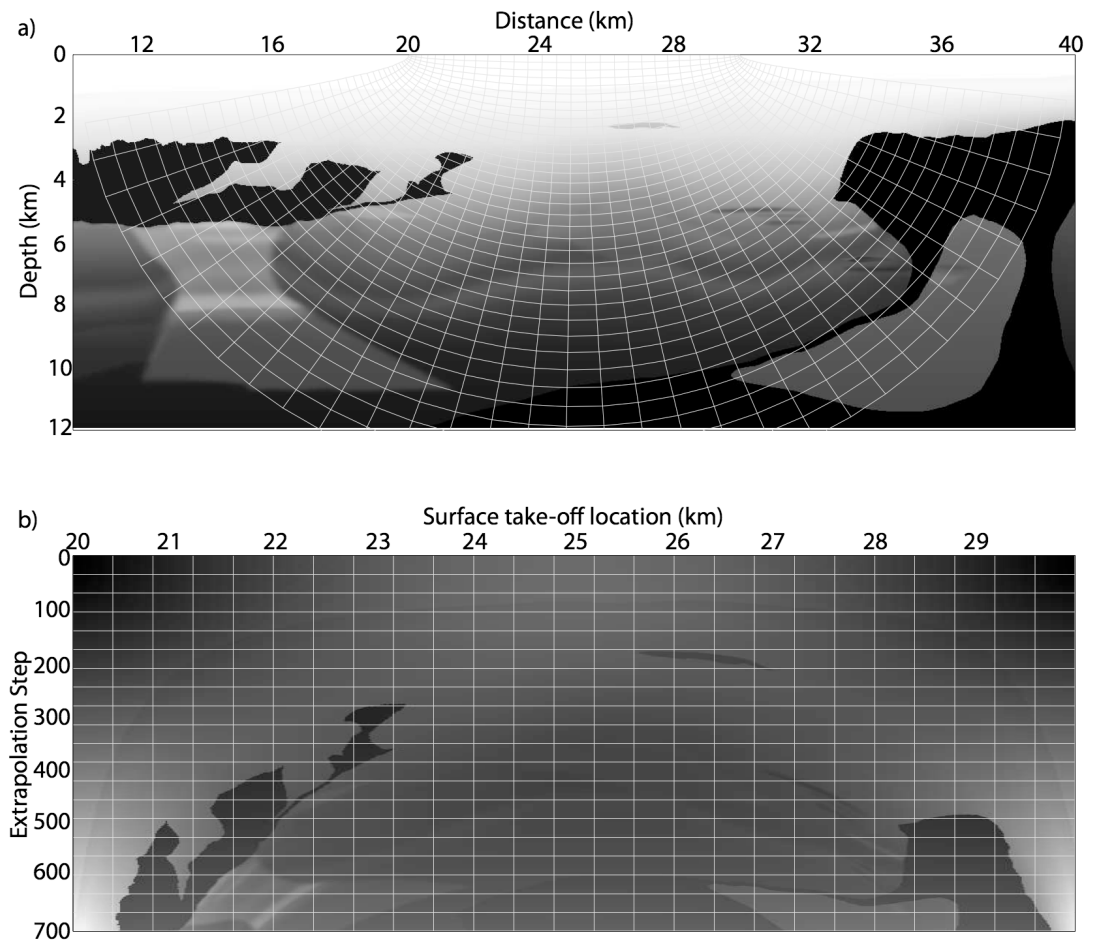


Figure 3.5: Prestack migration test in elliptical coordinates. a) Benchmark synthetic velocity model with the elliptical coordinate system overlain. b) Effective slowness model in the transformed elliptical coordinate system. **NR** georwe/. Figure5

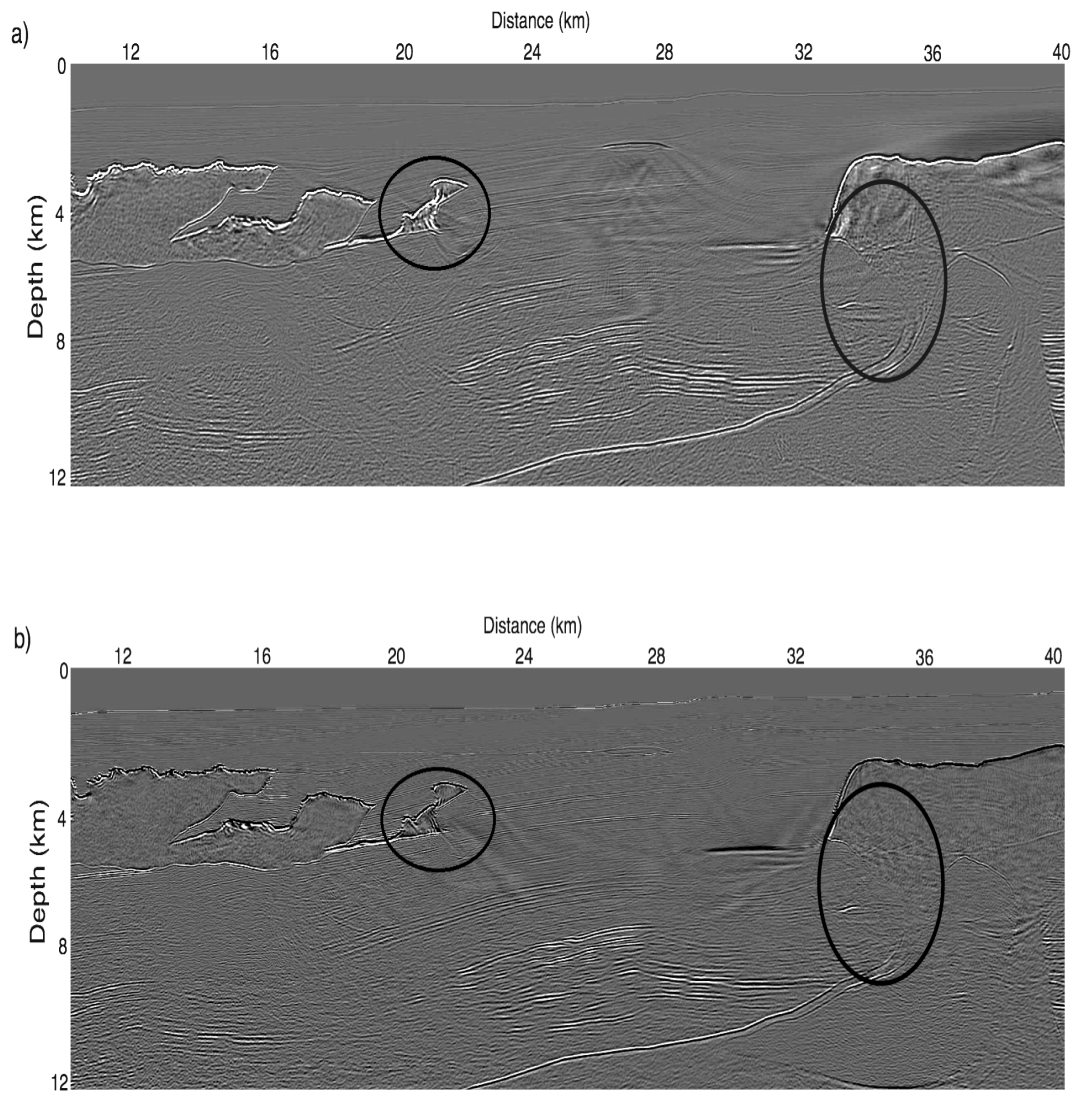


Figure 3.6: Synthetic migration results. a) Elliptical-coordinate migration result using finite-difference propagators. b) Cartesian migration result generated by finite-difference extrapolators of equivalent accuracy. **CR** georwe/. Figure6

Discussion

One question naturally arising when using RWE propagation in a prestack migration algorithm is how does one obtain the optimal trade-off between using i) low-order extrapolators on more dynamic coordinate systems (e.g. ray coordinates); and ii) high-order extrapolators on analytic meshes less conformal to the wavefield propagation direction. Based on experience, I argue that a parametric coordinate system (such as a tilted Cartesian or an elliptical mesh) offers the advantage of developing analytic extrapolation operators that readily lend themselves to high-order finite-difference schemes. While coordinate systems based on ray tracing better conform to the wavefield propagation direction, numerically generated meshes do not lend themselves as easily to high-order extrapolators because of the greater number, and spatially variability, of corresponding mixed-domain coefficients. In addition, analytic coordinates allow the user to specify a coordinate system adequate for propagating both the source and receiver wavefields, rather than optimizing for one or the other. One caveat, however, is that higher-order extrapolators are usually required for analytic coordinate systems because, though they are more optimal for global propagation, they are less conformal to the local extrapolation direction.

CONCLUSIONS

This chapter applies the Riemannian wavefield extrapolation on approach of Chapter 2 to 2D prestack shot-profile migration. I choose an elliptical coordinate system that generally conforms to the wave-propagation direction and enables large-angle extrapolation of both source and receiver wavefields. Post-stack migration results of a turning-wave data set validate the approach, while the 2D prestack imaging results show that the RWE migration algorithm generates images more accurate than the corresponding Cartesian algorithms. The cost difference between the elliptical and Cartesian imaging algorithms is only two additional interpolations per migrated shot profile. I argue that parametric coordinate systems are a good trade-off between the competing constraints of meshes conformal to the wavefield propagation direction and

coordinate system simplicity because one can readily develop analytic wavenumbers and more accurate high-order extrapolation implementations. Finally, I examine 2D elliptical-coordinate angle-domain common-image gathers in Chapter 4, and provide a 3D prestack migration extension of the analytic coordinate approach in Chapter 5.

ACKNOWLEDGMENTS

I thank Guojian Shan, Biondo Biondi, Ben Witten, Brad Artman, and Ken Larner for enlightening discussions. I acknowledge BP for the synthetic velocity data set. I also acknowledge the reviewers of the Geophysics manuscript and thank them for their helpful comments. Guojian Shan is a second author on the Geophysics paper.